

ELECTROCHEMISTRY

An ultrastable lithium metal anode enabled by designed metal fluoride spansules

Huadong Yuan^{1,2*}, Jianwei Nai^{1*}, He Tian^{3*}, Zhijin Ju¹, Wenkui Zhang¹, Yujing Liu¹, Xinyong Tao^{1†}, Xiong Wen (David) Lou^{2†}

The lithium metal anode (LMA) is considered as a promising star for next-generation high-energy density batteries but is still hampered by the severe growth of uncontrollable lithium dendrites. Here, we design “spansules” made of NaMg(Mn)F₃@C core@shell microstructures as the matrix for the LMA, which can offer a long-lasting release of functional ions into the electrolyte. By the assistance of cryogenic transmission electron microscopy, we reveal that an in situ–formed metal layer and a unique LiF-involved bilayer structure on the Li/electrolyte interface would be beneficial for effectively suppressing the growth of lithium dendrites. As a result, the spansule-modified anode affords a high Coulombic efficiency of 98% for over 1000 cycles at a current density of 2 mA cm⁻², which is the most stable LMA reported so far. When coupling this anode with the Li[Ni_{0.8}Co_{0.1}Mn_{0.1}]O₂ cathode, the practical full cell further exhibits highly improved capacity retention after 500 cycles.

INTRODUCTION

The high specific capacity of 3861 mAh g⁻¹ and ultralow electrochemical potential (–3.04 V versus standard hydrogen electrode) make the Li metal anode (LMA) a competitive candidate that can probably meet the ever-increasing requirement of high energy density for next-generation energy storage systems (1–5), especially in lithium-sulfur and lithium-oxygen batteries (6–8). However, the uncontrolled growth of Li dendrites (Fig. 1A), caused by uneven Li nucleation and unstable solid electrolyte interphase (SEI) during the Li plating/stripping processes, impedes the commercialization step of the LMA in practical uses for batteries (9–12). Unremitting efforts have been paid to address the Li dendrite issue by many physical and/or chemical strategies in the past decades (13–23). Constructing functional anodic hosts, such as three-dimensional porous frameworks (13–20) and lithiophilic group–decorated matrixes via alloying and/or acid–base pairing interactions (21–23), has recently been used as an effective approach to influence the nucleation and growth behaviors of plated Li and effectively suppress the growth of Li dendrites. The other approach is to stabilize the SEI. Strategies including the exploitation of electrolyte additives (24–28), artificial protection layers (29–32), and solid-state electrolytes (4, 33–36) have been developed to regulate and modify the physicochemical properties of the Li/electrolyte interface (37), leading to uniform Li⁺ ion flux distribution and thus stable Li electroplating. At present, most reported protocols, however, only focused on either inducing uniform Li nucleation or stabilizing the SEI. Exploiting compelling schemes that can realize the combination of these two paths for the development of stable LMAs is highly challenging.

Despite the efforts mentioned above, significant works that can enable the LMAs with a long cycle life more than 500 cycles at a high current density beyond 1 mA cm⁻² are still limited. One of the major reasons is that the lithiophilic groups and the electrolyte ad-

ditives are usually introduced into the battery systems via a one-time addition approach, whose amounts are generally optimized to maximize the effectiveness while avoiding unnecessary side reactions. The battery life would decay if the lithiophilic groups are shielded by dead Li or the electrolyte additives are consumed excessively after a certain number of cycles (21, 26, 28). Although the above facts are well recognized, the resupply of those ingredients would, however, encounter practical difficulties due to the leakproofness of battery systems during the cycling processes. Therefore, exploring a protocol that can provide a sustainable feed of the functional ingredients to maintain their amount at an appropriate and effective level for a long period is of critical importance toward the ultralong cycle life of the battery systems. Inspired from the metal alloying effect for guiding uniform Li deposition (38, 39) and the halides for stabilizing the SEI (35, 40, 41), introducing an electrolyte-soluble metal fluoride as the additive but sealed into a designed capsule to control its release rate into the electrolyte may be a revolutionary approach to realize long-term cycling for the LMAs. As illustrated in Fig. 1B, the metal ions released from the capsule may be in situ reduced to form a metal (M) layer, which is well covered on the surface of the substrate (e.g., Cu foil), where the Li deposition is expected to be dendrite free. Meanwhile, the continued release of fluoride ions should be in favor of the formation of a stable LiF-rich SEI throughout the cycling process.

Here, in our scheme, the effective ingredient is designed as a combination of electrolyte-soluble alkali metal fluoride with insoluble transition metal fluorides, that is NaMg(Mn)F₃ (NMMF) microcubes, to regulate its dissolution rate. Because of its electrochemically stable characteristic, carbon is selected as the protecting shell layer to further retard the dissolution rate of the fluorides. As expected, the carbon-coated NaMg(Mn)F₃ (NMMF@C) core@shell microstructures are found to act like “spansules” for the battery system, which offer a long-lasting release of functional metal and fluoride ions into the electrolyte. The in situ–formed M layer and the unique LiF-rich SEI layer structure were proved by the advanced cryogenic transmission electron microscopy (cryo-TEM) technique. The NMMF@C-modified LMA manifests an ultrastable performance with the highest Coulombic efficiency (CE) reported so far. When using the NMMF@C into the full-cell test, ultrahigh capacity retention and superior cycle

Copyright © 2020
The Authors, some
rights reserved;
exclusive licensee
American Association
for the Advancement
of Science. No claim to
original U.S. Government
Works. Distributed
under a Creative
Commons Attribution
NonCommercial
License 4.0 (CC BY-NC).

¹College of Materials Science and Engineering, Zhejiang University of Technology, Hangzhou 310014, China. ²School of Chemical and Biomedical Engineering, Nanyang Technological University, 62 Nanyang Drive, Singapore 637459, Singapore. ³Center of Electron Microscope, School of Materials Science and Engineering, Zhejiang University, 310027 Hangzhou, China.

*These authors contributed equally to this work.

†Corresponding author. Email: tao@zjut.edu.cn (X.T.); xwlou@ntu.edu.sg (X.W.L.)

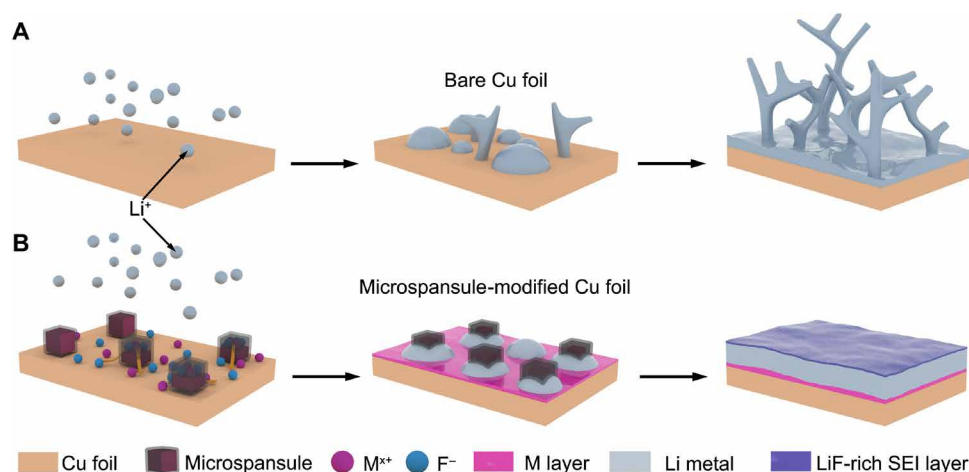


Fig. 1. Schematic illustration of the expected growth behavior of Li when plating on bare Cu foil and microspansule-modified Cu foil. (A) Behavior of Li nucleation and dendrite growth during Li plating on bare Cu foil. (B) Upon Li plating on microspansule-modified Cu foil, the in situ formation of M layer derived from dissolved metal ions of microspansules can effectively guide dendrite-free Li deposition. Meanwhile, with the concurrent supply of fluoride ions, a steady and LiF-rich SEI is formed outside the plated Li, leading to a uniform distribution of Li⁺ ion flux and stable Li electroplating.

life can also be realized, demonstrating its feasibility for the use in practical batteries.

RESULTS

Characterization of the obtained NMMF@C spansules

The NMMF@C microcubes were synthesized via a facile method in large scale (Fig. 2A), including precipitation of fluorides (NMMF), coating with resin, and carbonization (details can be found in the Supplementary Materials). The powder x-ray diffraction (XRD) pattern of the obtained NMMF@C sample (Fig. 2B) indicates that the fluoride component is a composite and made of two phases, that is, the orthorhombic phases of NaMgF₃ (JCPDS card no. 13-0303) and NaMnF₃ (JCPDS card no. 18-1224). Field-emission scanning electron microscopy (FESEM) and TEM were used to characterize the morphology and microstructure of the obtained NMMF and NMMF@C. The FESEM image reveals that the NMMF has a cubic shape with a smooth surface and an average size of ~500 nm (Fig. 2C). After coating the NMMF with carbon, the obtained NMMF@C still remains a cubic morphology (Fig. 2, D and E). High-resolution TEM (HRTEM) image exhibits an interplanar distance of 3.4 Å, corresponding to the *d* spacing of the (002) plane of graphite (inset of Fig. 2E). The core@shell structure of an individual NMMF@C cube can be clearly discerned under the scanning TEM (STEM) mode, by which the thickness of the shell layer is determined to be ~30 nm (Fig. 2F). The elemental mapping results (Fig. 2F) of a representative cube further confirm the elemental composition and distribution within the NMMF@C core@shell structures. It is noticed that the Mn is located in the central region of the cube, while the Mg is in the periphery region.

Deposition behavior of Li metal and the structure of SEI

The Li deposition behaviors on bare Cu foil (b-Cu) and NMMF@C-modified Cu foil (NMMF@C-Cu) were investigated using the FESEM technique. Figure 3A shows a top view of the Li film that is electrodeposited on the NMMF@C-Cu with a plating capacity of 0.5 mAh cm⁻² at the current density of 0.5 mA cm⁻². Compared with

uncontrolled growth of Li dendrites on the b-Cu (fig. S1), Li metal is uniformly plated on the NMMF@C-Cu (inset of Fig. 3A), particularly around the NMMF@C cubes (fig. S2). In addition, the related cross-sectional FESEM image (Fig. 3B) also shows the tight contact between the plated Li metal and NMMF@C cubes. Notably, the plated Li would fuse together and continuously enter the inner space of the NMMF@C-modified layer without any Li dendrites present on the anode even when the plating capacity reached to 1 and 3 mAh cm⁻² (Fig. 3, C to F). In addition, the uniform deposition of Li can also be found on the NMMF-Cu substrate (fig. S3). These observations imply that the NMMF should be the key to guide the dendrite-free Li deposition regardless of the carbon coating. Hollow structures observed from the TEM and related elemental mapping images of the NMMF@C sample confirm the dissolvable nature of the NMMF in the electrolyte (fig. S4), which is further verified by the XRD results (fig. S5). The role of the carbon coating of the NMMF@C was investigated by comparing the morphological differences between the NMMF@C and NMMF after soaking them in the electrolyte for a same period of 48 hours (figs. S4 and S6). It is clearly revealed that the dissolution rate of NMMF in the electrolyte is significantly reduced with the protection of the carbon shell. This reduced dissolution can also be proved by measuring the concentration of various metal ions in the NMMF- and NMMF@C-soaked electrolyte from the inductively coupled plasma mass spectrometry (ICP-MS) experiments (fig. S7). The detailed dissolution behavior of the NMMF@C in this system was further investigated (fig. S8 and table S1). The results show that the mass loss of the NMMF@C is nearly linear as a function of time, with a calculated mass loss rate of ~0.06 weight % (wt %) h⁻¹. This indicates that a highly stable releasing rate of the functional ingredients could be realized by these NMMF@C-based spansules. In addition, the high stability of the carbon shell as the spansule skin can largely avoid some possible side reactions with the ether electrolyte and thus improve the reversible utilization of the plated Li. The relatively high conductivity of the carbon shell may also facilitate the uniform deposition of Li on the NMMF@C-modified electrode.

On the basis of the above results, we propose that the reduced dissolution rate of NMMF is anticipated to be beneficial for a continuous

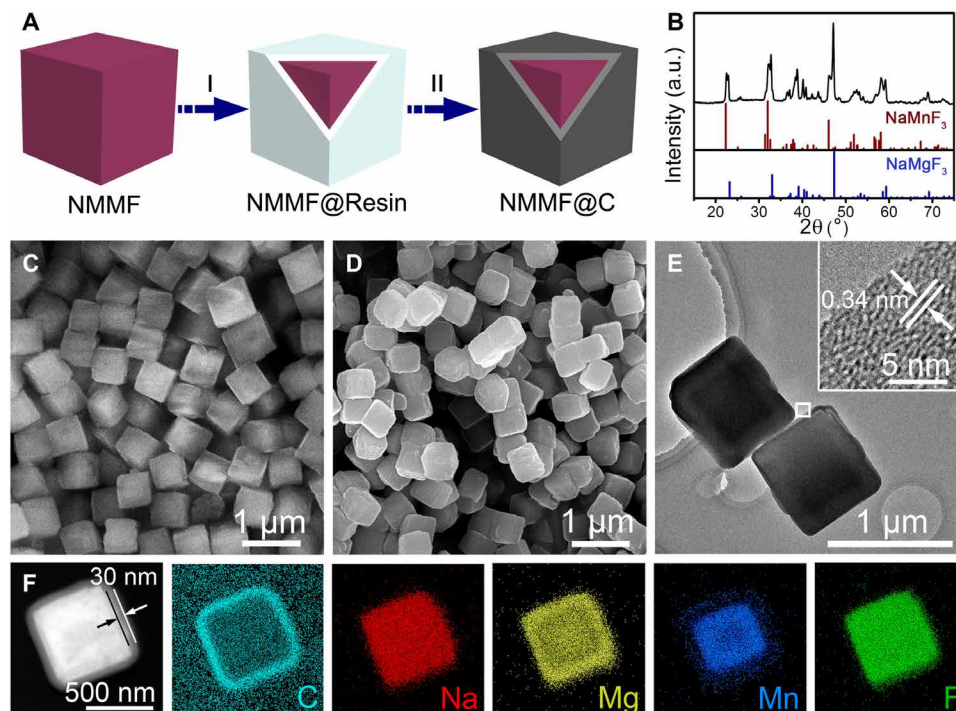


Fig. 2. Fabrication strategy and characterizations of the NMMF@C microcubes. (A) Synthetic scheme of the NMMF@C cubes, which includes two steps: I, coating resorcinol-formaldehyde resin on the as-prepared cubes; II, carbonization at high temperature. (B) XRD pattern of the NMMF@C cubes together with two standard patterns. a.u., arbitrary units. (C) FESEM image of the NMMF cubes. (D) FESEM image of NMMF@C cubes. (E) TEM images of the NMMF@C cubes. Inset is a HRTEM image taken from the region indicated by a white square. (F) STEM and elemental mapping images of the Na, Mg, C, Mn, and F elements of a single NMMF@C cube.

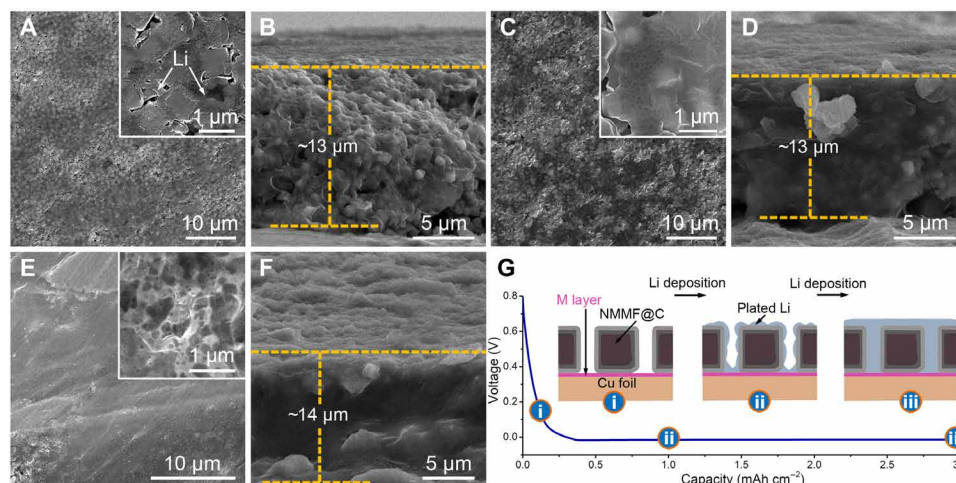


Fig. 3. The deposition behavior of the Li plated on the NMMF@C-Cu. (A) Top and (B) cross-sectional images of Li plated with a capacity of 0.5 mAh cm^{-2} . (C) Top and (D) cross-sectional images of Li plated with a capacity of 1 mAh cm^{-2} . (E) Top and (F) cross-sectional images of Li plated with a capacity of 3 mAh cm^{-2} . (G) The staged discharge curve of the NMMF@C-Cu anode and the corresponding schematic diagram of Li plating processes on the NMMF@C-Cu.

release of functional ions (Na^+ , Mg^{2+} , Mn^{2+} , and F^-) and thus prolonging their working duration. As shown in the schematic diagram, the Li metal plating process on NMMF@C-Cu might be understood as three stages (Fig. 3G): (i) Because of the higher redox potentials of Mn/Mn^{2+} (1.87 V versus Li/Li^+) (42), Mg/Mg^{2+} (0.85 V versus Li/Li^+) (43, 44), and Na/Na^+ (0.28 V versus Li/Li^+) (27) than Li/Li^+ (fig. S9), the dissolved metal ions (Na^+ , Mg^{2+} , and Mn^{2+}) will be in situ reduced to form an M layer on the matrix surface during the initial discharge process before

the start of Li deposition (fig. S10), which has been further proved by the x-ray photoelectron spectroscopy (XPS) sputter etching measurement (fig. S11). (ii) The plated Li metal would be uniformly nucleated on the matrix surface by the guidance of the M layer. (iii) With the increase of Li plating capacity, the Li metal gradually fills into the internal space of the NMMF@C layer without growing any dendrites.

To further understand the effect of those released ions (Na^+ , Mg^{2+} , Mn^{2+} , and F^-) for protecting the LMA, we used the cryo-TEM

technique, which was developed recently for observing Li metal and SEI constituent (45–47), to uncover their functionalization mechanism. As shown in Fig. 4A, Li dendrites were grown on a bare Cu grid with a capacity of 0.5 mAh cm^{-2} at the current density of 0.5 mA cm^{-2} . In contrast, no dendrites were observed on the NMMF@C-modified Cu grid (Fig. 4, B and C, and fig. S12). The deposited Li is spherical and seems to nucleate preferentially around the NMMF@C cubes, which is in agreement with that observed in the FESEM images (fig. S2). Related elemental mapping images and the detected nanograins corresponding to metallic Na, Mg, and Mn further confirm the formation of the M layer on the Cu grid/NMMF@C interfaces (Fig. 4D and fig. S13), which could guide the dendrite-free growth of the Li metal. As revealed by an HRTEM image obtained from the sample that deposited on the bare Cu grid (Fig. 4E, corresponding to the white rectangular area in Fig. 4A), the lattice fringes and the fast Fourier transform (FFT) image match well with the (110) planes of the metallic Li, confirming that the electroplated product is crystalline Li [area (1)]. The SEI layer on the Li shows a typical mosaic structure (Fig. 4E) (45, 46), specifically, crystalline Li_2O nanoparticles recognized by the matched lattice spacings of the (111) planes [area (2)] are dispersed in amorphous SEI matrix. This indicates that the SEI is composed of unevenly distributed inorganic and organic components. Crystalline Li metal is also verified from the sample grown on the NMMF@C-modified Cu grid [area (1) in Fig. 4F]. In addition, instead of the single-layer mosaic structure, the SEI here exhibits a bilayered structure (Fig. 4F, corresponding to the white rectangular area in Fig. 4B), specifically, crystalline granular Li_2O -involved mosaic structure as the inner layer and ordered laminar Li_2O as the outer layer [area (2)]. LiF nanograins can also be detected in the inner layer of the SEI [area (3), and the FFT image shown in Fig. 4G]. These locations of Li_2O and LiF could also be confirmed by the vertical distribution of elemental O and F detected by XPS (fig. S11). Furthermore, XPS and energy-

dispersive x-ray (EDX) spectroscopy results confirm that the LiF content in the SEI from the NMMF@C-Cu sample is much higher than that from the bare Cu sample (figs. S14 and S15). This LiF-rich SEI is believed to enable the stabilization of the Li/electrolyte interface and thus uniform Li electroplating (4).

Electrochemical performance of the electrodes in half- and full-cell configurations

The CE is a crucial parameter to evaluate the sustainability and practicality of the LMAs, which is defined as the ratio of stripped capacity to plated capacity (48). The typical coin cells of bare Li coupled with different Cu-based anodes (NMMF@C-Cu, NMMF-Cu, and b-Cu) were assembled to conduct the CE measurement. The results plotted as CE versus cycle number of cells at different current densities with the same plating capacity of 1 mAh cm^{-2} are shown in Fig. 5A. Compared with the b-Cu and NMMF-Cu, the NMMF@C-Cu anode delivers more stable electrochemical cycling and longer cycle life. To be specific, the NMMF@C-Cu anode exhibits a stable CE around 98.5% for more than 600 cycles under the current density of 1 mA cm^{-2} . Note that some processes such as the M-Li alloying and Li^+ intercalation into the carbon shell could exist during all the cycles (fig. S16), which might reduce the CE of the NMMF@C-Cu electrode especially in the initial cycles. Nevertheless, the CE will be significantly improved in the following hundreds of cycles due to the formation of stable LiF-rich SEI and dendrite-free growth of Li metal. In comparison, the NMMF-Cu and b-Cu anodes show much poorer cycle life with less than 200 and 80 cycles, respectively. In addition, when NaF, which would be fully dissolved fast in the electrolyte, is used as the exclusive additive, the LMA on b-Cu shows better cycle life (fig. S17), but it is still much poorer than that of the NMMF-Cu and NMMF@C-Cu (Fig. 5A). These data prove that the designed slow release of the functional ions is of great importance for improving the stability of the LMAs. As the current density

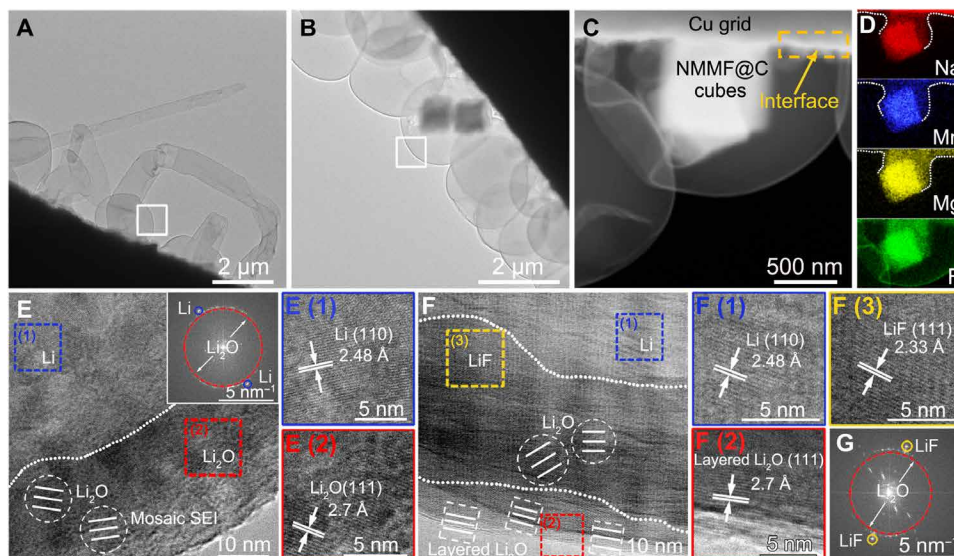


Fig. 4. Cryo-TEM study on the anode structure. (A) Morphology of Li plated on a bare Cu grid. (B and C) Morphology of Li plated on the NMMF@C-modified Cu grid. (D) Elemental mapping images of the Na, Mg, Mn, and F. (E) HRTEM and related FFT images of the SEI formed on bare Cu grid [corresponding to the white rectangular area in (A)], E (1) and E (2) correspond to regions (1) and (2) in (E), respectively. (F) HRTEM image of the SEI formed on NMMF@C-modified Cu grid [corresponding to the white rectangular area in (B)], F (1), F (2), and F (3) correspond to regions (1), (2), and (3) in (F), respectively. (G) FFT data from the image of (F), confirming the existence of LiF in the SEI layer.

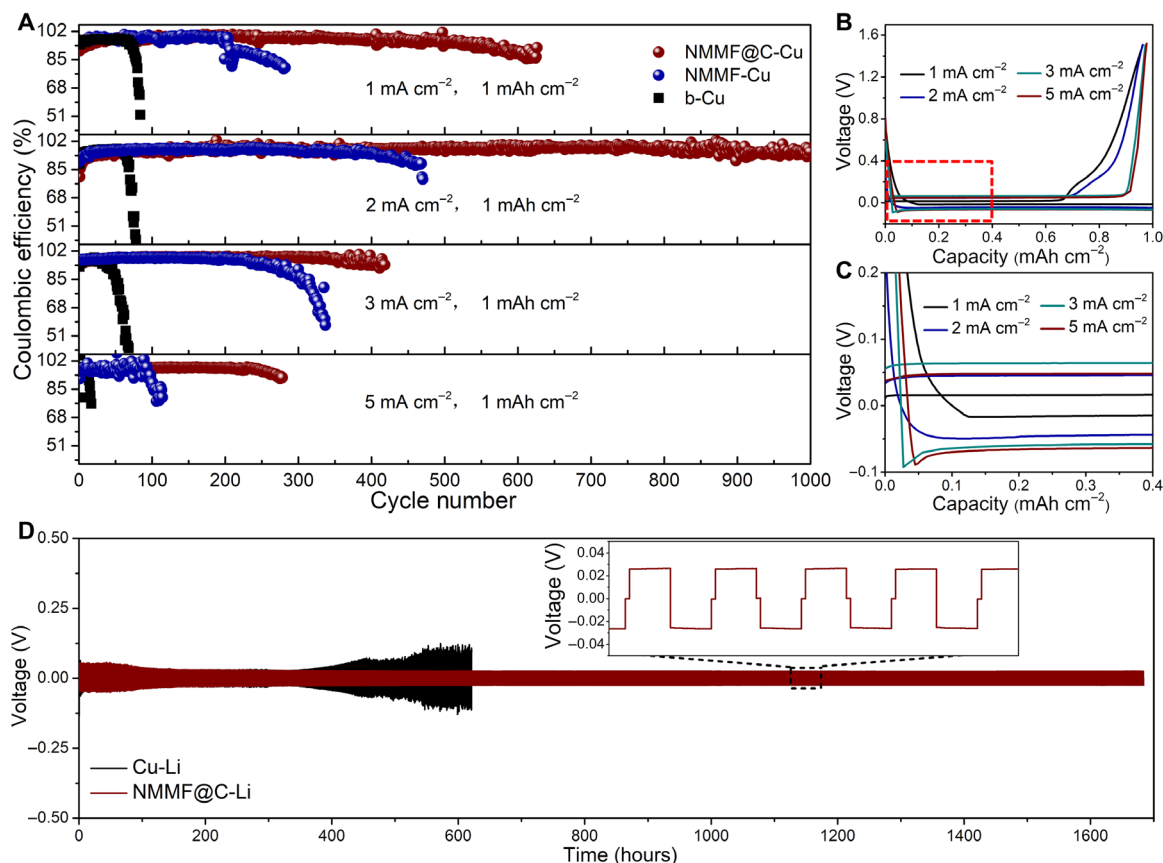


Fig. 5. Electrochemical performance of different anodes in the half cells with the ether electrolyte. (A) CE versus cycle number plots of the anodes based on NMMF@C-Cu, NMMF-Cu, and b-Cu. **(B)** Electrochemical Li plating/stripping curves of the NMMF@C-Cu anode at 1 mA cm^{-2} with a specific capacity of 1 mAh cm^{-2} . **(C)** Magnification of the red rectangular region in (B). **(D)** Galvanostatic discharge/charge voltage curves of Cu-Li and NMMF@C-Li anodes in symmetric coin cells at 1 mA cm^{-2} .

increases to 2 mA cm^{-2} , the NMMF@C-Cu anode achieves a high CE of 98% for more than 1000 cycles, while the CE of NMMF-Cu and b-Cu drops below 85% after only 450 and 70 cycles, respectively (Fig. 5A). Although the NMMF@C anode shows a larger cycle number at 2 mA cm^{-2} than at 1 mA cm^{-2} , the lifetime at 2 mA cm^{-2} is shorter than that at 1 mA cm^{-2} (fig. S18). To the best of our knowledge, this stable CE of the NMMF@C-Cu obtained under the high current density of 2 mA cm^{-2} for more than 48 days is one of the longest cycle lives in ether-based electrolytes reported so far (table S2). It should be mentioned that the loading thickness of the NMMF@C particles on the electrode is also very important for stable Li plating/stripping. A cycle life of about only 450 cycles can be obtained when the thickness is reduced from the typical value of $13 \mu\text{m}$ (Fig. 3B) to $6.5 \mu\text{m}$ (fig. S19). The exhaust of effective ingredients after 450 cycles should account for this shorter cycle life. On the other hand, when the thickness is increased to $27.5 \mu\text{m}$, the cycle life could maintain for only 300 cycles (fig. S19). This may be attributed to the excessive consumption of electrolyte by the very high content of the released reactive ions. Therefore, the optimal thickness of NMMF@C loaded on the electrode is found around $13 \mu\text{m}$ (Fig. 3B).

In further tests, the NMMF@C-Cu anode can still achieve a high CE close to 98% for more than 400 and 200 cycles even at much higher current densities of 3 and 5 mA cm^{-2} , respectively, exhibiting superior stability than those of the NMMF-Cu and b-Cu. Notably,

under a high plating capacity of 5 mAh cm^{-2} , the CE of the NMMF@C-Cu electrode is maintained at $\sim 96\%$ for more than 140 and 80 cycles at the current densities of 5 and 1 mA cm^{-2} , respectively (fig. S20A). When increasing the plating capacity to even 7 mAh cm^{-2} , the CE can be stable at $\sim 96\%$ after 100 and 60 cycles at 7 and 1 mA cm^{-2} , respectively (fig. S20B). The nucleation overpotential of the NMMF@C-Cu is calculated from the Li plating/stripping voltage curves (Fig. 5, B and C). The values are around 0, 0.22, and 30 mV for the current densities of 1, 2, 3, and 5 mA cm^{-2} , respectively (fig. S21). These ultralow nucleation overpotentials indicate the super lithiophilicity of the NMMF@C, especially when the current density is less than 2 mA cm^{-2} . A nearly zero nucleation overpotential value indicates that the formed M layer on the matrix surface may react with Li before actual formation of the metallic Li phase, which can effectively inhibit the growth of Li dendrites. Electrochemical impedance spectroscopy (EIS) was performed to analyze the inner resistance and interfacial stability (fig. S22). After 1 cycle, the cell with the NMMF@C-Cu anode exhibits a lower interfacial resistance than the b-Cu anode. After 50 cycles, the increase in size of the semicircle at high frequency suggests the increased thickness of the resistive SEI layer in the b-Cu electrode. In contrast, the reduced semicircle size at high frequency of the NMMF@C-Cu-based cell implies the stable surface of the electrode.

To investigate the interfacial stability and Li^+ ion transport capability, we preplated Li on the NMMF@C-Cu (NMMF@C-Li) with a

capacity of 3 mAh cm^{-2} and assembled a symmetric NMMF@C-Li/separator/NMMF@C-Li cell in the same ether electrolyte. This symmetric cell exhibits a flat Li stripping/plating plateau with a small overpotential of 20 mV beyond 800 cycles for more than 1600 hours (Fig. 5D). The possible “soft short circuit” (49) at such a low overpotential can be ruled out by comprehensive measurements of the activation energy, the EIS plots of the symmetric cell, and the open-circuit voltage, as well as the morphological observations of the plated Li and the used separator after longtime cycling (figs. S23 to S26). In contrast, the symmetric cell using b-Cu electrodes plated with the same amount of Li displays an erratic voltage, where the overpotential increases after 400 hours and then fluctuates. Therefore, the stable cycle life and low polarization potential of the symmetric cell suggest that the NMMF@C-Li anode is capable of working under practical cycling conditions.

To demonstrate the potential application of the NMMF@C-Li anode in practical batteries, the NMMF@C-Li anode was paired with a $\text{Li}[\text{Ni}_{0.8}\text{Co}_{0.1}\text{Mn}_{0.1}]\text{O}_2$ (NCM811) cathode to obtain a full cell (NCM811/NMMF@C-Li). In addition, a full cell using the same NCM811 cathode and a b-Cu anode (NCM811/Cu-Li) was also assembled for comparison. Figure 6A shows the discharge/charge voltage profiles of the NCM811/NMMF@C-Li full cell at different current densities. Compared with the full cell using a Cu-Li anode (fig. S27), the NCM811/NMMF@C-Li cell exhibits lower polarization potential in both the charge and discharge processes. In addition, the rate performance of NCM811/NMMF@C-Li is better than that of the NCM811/Cu-Li (Fig. 6B and fig. S28). The discharge specific capacities of NCM811/NMMF@C-Li are 224, 193, 178, 164, and 147 mAh g^{-1} corresponding to the increasing current density from

0.2 to 3 C (Fig. 6B). When the current density returns to 0.5 C, the reversible capacity recovers to 191 mAh g^{-1} , indicating the superior stability of the NCM811/NMMF@C-Li cell. Besides the rate performance, the long-term cycling performance of NCM811/NMMF@C-Li was investigated at the current density of 1 C. As illustrated in Fig. 6C, the NCM811/NMMF@C-Li full cell shows a higher initial capacity of 192 mAh g^{-1} , and it maintains at 130 mAh g^{-1} even after 500 cycles, with an ultralow capacity decay rate of 0.06% per cycle. Compared with the previous reported full cells using NCM-based cathodes (50–52), the NCM811/NMMF@C-Li cell gives one of the most stable cycle lives reported so far, which suggests the feasibility of using the NMMF@C-Li anodes for practical Li batteries.

DISCUSSION

In summary, we have successfully designed a smart sparsule structure based on the carbon-coated mixed metal fluoride (NMMF@C) core/shell microparticles to provide a long and sustainable supply of effective ingredients in the electrochemical system for stabilizing the lithium metal anodes. It is found that the NMMF core would gradually dissolve and release functional metal and fluoride ions into the electrolyte during the Li plating/stripping cycles, in which the release rate could be efficaciously reduced by the carbon shell. With the assistance of the cryo-TEM measurements, a metal layer is found to be formed in situ on the surface of the Cu substrate that is believed to be able to guide uniform Li deposition. Meanwhile, a unique LiF-involved bilayer SEI structure was observed and believed to stabilize the Li/electrolyte interface, leading to uniform Li^+ flux and significantly improving the stability of the anode when

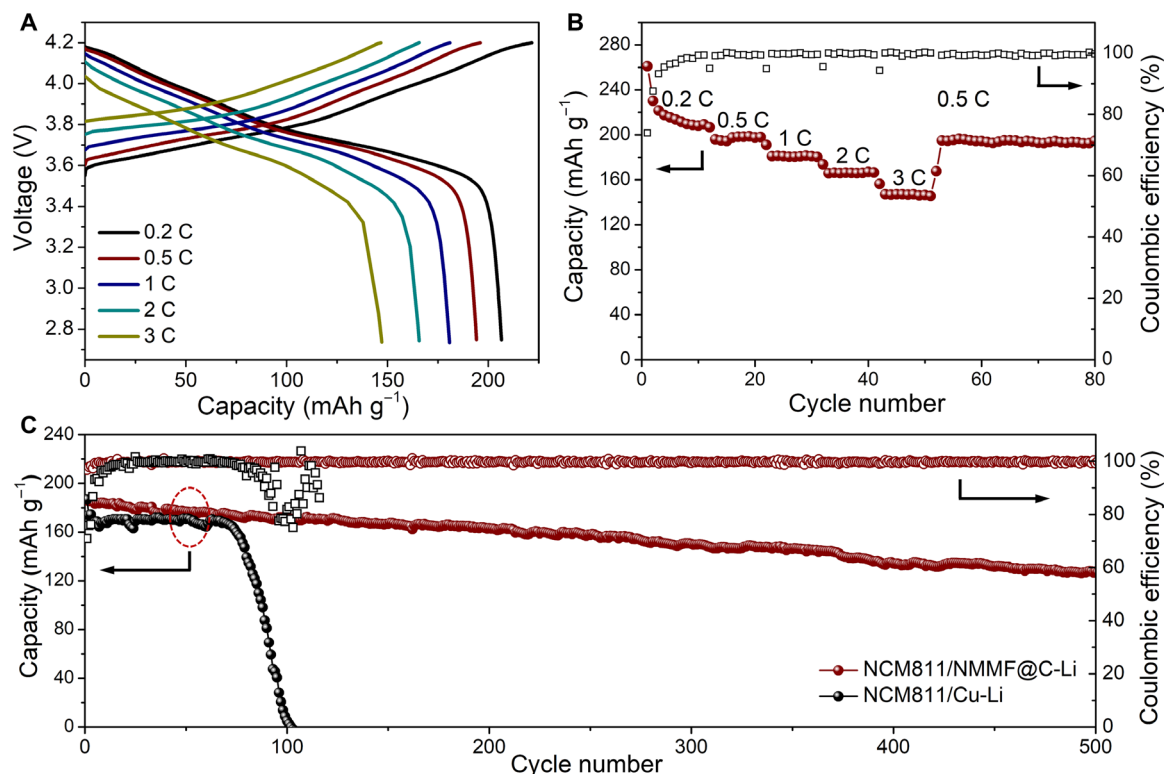


Fig. 6. Electrochemical performance of full cells. (A) Discharge/charge voltage profiles of the NCM811/NMMF@C-Li full cell at different current densities. (B) Rate capability of the NCM811/NMMF@C-Li full cell. (C) Long-term cycling performance of NCM811/NMMF@C-Li and NCM811/Cu-Li cells at the current density of 1 C.

electroplating Li. Benefitting from these merits, a high CE around 98% is achieved for more than 1000 cycles with the capacity of 1 mAh cm^{-2} at the high current density of 2 mA cm^{-2} . A full cell assembled from the NCM811 cathode and the NMMF@C-Li anode exhibits high initial capacity and ultralow capacity decay rate of 0.06% per cycle after 500 cycles at 1 C. These remarkable properties enable the NMMF@C microparticles to be a highly promising matrix material for the lithium metal anodes. We anticipate that the present work might represent an important breakthrough toward the practical use of lithium metal anodes in rechargeable batteries.

MATERIALS AND METHODS

Fabrication of NMMF

In a typical synthesis of NMMF nanocubes, 6.4 mmol of magnesium acetate and 1.6 mmol of manganese acetate were successively dissolved into a mixed solution containing 10 ml of water and 10 ml of ethanol. Next, 40 ml of aqueous solution dissolved with 0.028 mol of sodium fluoride was added dropwise into the above solution with continuous stirring. After stirring for 60 min, the mixed solution was then maintained for 24 hours at room temperature. The as-obtained NMMF was collected through centrifugation, washed with water and ethanol to remove impurities, and finally dried at 60°C for 6 hours.

Fabrication of NMMF@C

First, 100 mg of NMMF nanoparticles was dispersed in a mixed solution of 20 ml of deionized water and 40 ml of ethanol via ultrasonication and stirring. Then, 1.2 g of ammonia solution (28 wt %), 0.2 g of resorcinol, and 0.2 g of formaldehyde (37 wt %) were successively added into the above solution, and the mixed dispersion was mechanically stirred for 12 hours at room temperature. Last, the obtained NMMF nanocubes coated with resorcinol-formaldehyde resin (NMMF@Resin) were isolated by centrifugation and washed using deionized water and ethanol several times. After the carbonization process at 800°C in Ar atmosphere with a heating rate of 5°C min^{-1} , the NMMF@C sample was obtained.

Cryo-TEM sample preparation process

Here, bare Cu grid (used in TEM measurement) and NMMF@C-modified Cu grid were used as matrix for Li deposition. The plated Li amount was 0.5 mAh cm^{-2} at the current density of 0.5 mA cm^{-2} . Once the samples were washed using dioxolane and dried, it was transferred into the cryo-TEM holder in an Ar-filled glove box. Using a sealed container, the cryo-TEM holder was quickly inserted into FEI Talos-S, and then, liquid nitrogen was poured into the cryo-TEM holder until the sample temperature dropped below -170°C . All cryo-TEM images were taken at cryogenic temperatures (-170°C).

Electrochemical measurements

All coin cells were assembled using standard CR2032 coin-type cells in a glove box filled with Ar gas. To evaluate the electrochemical Li plating/stripping behavior, the electrodes (NMMF@C-Cu) used here were fabricated via mixing NMMF@C and poly(vinylidene difluoride) (PVDF) in a weight ratio of 8:2 using methyl-2-pyrrolidinone as a solvent. All electrodes had an area of 1.13 cm^2 . In addition, 1 M lithium bis(trifluoromethanesulfonyl)imide in dioxolane/dimethoxyethane (DOL/DME) (1:1, v/v) with 1 wt % lithium nitrate was used as the electrolyte. Note that the electrolyte used in each cell was controlled to be about 50 μl . For symmetric cell testing, NMMF@C-Cu plated

with 3 mAh cm^{-2} at the current density of 0.5 mA cm^{-2} served as the working electrode. Full cells using NCM811 as the cathode and NMMF@C-Li as the anode were assembled to evaluate the cycling stability of NMMF@C-Cu in practical battery systems. The NCM811 cathode was prepared by mixing NCM811, Super-P, and PVDF with a mass ratio of 8:1:1. The mass loading of the NCM811 cathode ranged from 4.5 to 5 mg cm^{-2} . The working potential window of the full cell was from 2.75 to 4.2 V. The electrolyte used in full cells was 1 M lithium hexafluorophosphate in 1:1 (v/v) ethylene carbonate and dimethyl carbonate with 1% vinylene carbonate and 10% fluoroethylene carbonate as additives, and the separator was Celgard 2325.

Materials characterizations

Powder XRD analysis [X'Pert Pro diffractometer using $\text{CuK}\alpha$ radiation ($\lambda = 0.15418 \text{ nm}$)] of different samples was carried out to investigate the crystalline phase of the synthesized samples. The morphology and microstructure of these samples including NMMF, NMMF@C, and the behavior of lithium deposition were observed by FESEM (Nova NanoSEM450). Elemental analysis was conducted on an EDX spectrometer attached to FESEM. XPS analysis was performed using Al $\text{K}\alpha$ (1486.6 eV) monochromatic x-ray source (AXIS Ultra DLD, Kratos). The concentration of metal ions was measured using ICP-MS with PerkinElmer ELAN DRC-e. In addition, the microstructures of samples, deposited Li metal, and SEI were carried out using TEM (FEI Talos-S), and cryo-TEM characterizations were carried out using Gatan 698 cryo-transfer holder.

SUPPLEMENTARY MATERIALS

Supplementary material for this article is available at <http://advances.sciencemag.org/cgi/content/full/6/10/eaaz3112/DC1>

Fig. S1. FESEM images of the Li plated on bare Cu foil.

Fig. S2. FESEM images of the Li plated on the NMMF@C-Cu with the capacity of 0.5 mAh cm^{-2} at the current density of 0.5 mA cm^{-2} .

Fig. S3. FESEM images of the Li plated on the NMMF-Cu.

Fig. S4. Characterizations of the NMMF@C cubes after soaking in the ether electrolyte (DOL/DME) for 48 hours.

Fig. S5. XRD patterns of the NMMF@C before and after soaking in the ether electrolyte.

Fig. S6. Characterizations of the NMMF cubes after soaking in the ether electrolyte for 48 hours.

Fig. S7. ICP-MS results showing the concentration of various metal ions in the ether electrolyte for the same period.

Fig. S8. The dissolution behavior of NMMF@C as a function of time in the ether electrolyte.

Fig. S9. The initial discharge curve of the NMMF@C-Cu anode during the activation process at the current density of 50 mA g^{-1} .

Fig. S10. FESEM and elemental mapping images of Li plating on b-Cu with several NMMF@C particles.

Fig. S11. A depth profiling of the elements on the Li-plated NMMF@C sample with a capacity of 0.5 mAh cm^{-2} by XPS sputter etching technique.

Fig. S12. A cryo-TEM image of the Li deposited on the NMMF@C-modified Cu grid.

Fig. S13. Cryo-TEM characterization for the M layer.

Fig. S14. XPS characterization.

Fig. S15. EDX characterization.

Fig. S16. Electrochemical Li plating curves on NMMF@C-Cu anodes at 1 mA cm^{-2} for 1 mAh cm^{-2} during the 100th, 200th, 300th, 400th, and 500th cycles.

Fig. S17. The CE versus cycle number plot of the LMA on b-Cu using NaF as the electrolyte additive.

Fig. S18. The cycle life of the NMMF@C-Cu electrode at the current densities of 1 and 2 mA cm^{-2} .

Fig. S19. Morphology and electrochemical performance of the Cu electrodes with different loading thickness of NMMF@C.

Fig. S20. The CE of Li deposition/stripping on the NMMF@C-Cu electrode at high areal capacities.

Fig. S21. Nucleation overpotential and polarization potential.

Fig. S22. The EIS plots of the NMMF@C-Cu and b-Cu electrodes after the 1st and 50th cycles.

Fig. S23. Arrhenius plot of the symmetric NMMF@C-Li//NMMF@C-Li cell.

Fig. S24. EIS plots of the symmetric cell at 1 mA cm^{-2} for 1 mAh cm^{-2} .
 Fig. S25. The first charge curves of three NCM811/NMMF@C-Li full cells at the current density of 100 mA g^{-1} .
 Fig. S26. FESEM images of the plated Li and separator in a symmetric cell after 400 cycles.
 Fig. S27. Charge/discharge curves of full cells.
 Fig. S28. Rate capability of the NCM811/Cu-Li full cell.
 Table S1. The mass loss of NMMF@C in the ether electrolyte as a function of time.
 Table S2. The comparison of the CE of the anode in our work and some reported state-of-the-art anodes tested in the DOL/DME ether electrolyte.
 References (53–57)

REFERENCES AND NOTES

- L. Li, S. Basu, Y. Wang, Z. Chen, P. Hundekar, B. Wang, J. Shi, Y. Shi, S. Narayanan, N. Koratkar, Self-heating-induced healing of lithium dendrites. *Science* **359**, 1513–1516 (2018).
- J. Liu, Z. Bao, Y. Cui, E. J. Dufek, J. B. Goodenough, P. Khalifah, Q. Li, B. Y. Liaw, P. Liu, A. Manthiram, Y. S. Meng, V. R. Subramanian, M. F. Toney, V. V. Viswanathan, M. S. Whittingham, J. Xiao, W. Xu, J. Yang, X.-Q. Yang, J.-G. Zhang, Pathways for practical high-energy long-cycling lithium metal batteries. *Nat. Energy* **4**, 180–186 (2019).
- M. D. Tikekar, S. Choudhury, Z. Tu, L. A. Archer, Design principles for electrolytes and interfaces for stable lithium-metal batteries. *Nat. Energy* **1**, 16114–16121 (2016).
- Y. Lu, Z. Tu, L. A. Archer, Stable lithium electrodeposition in liquid and nanoporous solid electrolytes. *Nat. Mater.* **13**, 961–969 (2014).
- D. Lin, Y. Liu, Y. Cui, Reviving the lithium metal anode for high-energy batteries. *Nat. Nanotechnol.* **12**, 194–206 (2017).
- W.-J. Kwak, S.-J. Park, H.-G. Jung, Y.-K. Sun, Optimized concentration of redox mediator and surface protection of Li metal for maintenance of high energy efficiency in Li-O₂ batteries. *Adv. Energy Mater.* **8**, 1702258 (2018).
- Z. Li, H. B. Wu, X. W. Lou, Rational designs and engineering of hollow micro-/nanostructures as sulfur hosts for advanced lithium-sulfur batteries. *Energy Environ. Sci.* **9**, 3061–3070 (2016).
- Z. Li, J. Zhang, B. Guan, D. Wang, L.-M. Liu, X. W. Lou, A sulfur host based on titanium monoxide@carbon hollow spheres for advanced lithium-sulfur batteries. *Nat. Commun.* **7**, 13065 (2016).
- X. Liang, Q. Pang, I. R. Kochetkov, M. S. Sempere, H. Huang, X. Sun, L. F. Nazar, A facile surface chemistry route to a stabilized lithium metal anode. *Nat. Energy* **2**, 17119 (2017).
- Y. Liu, Q. Liu, L. Xin, Y. Liu, F. Yang, E. A. Stach, J. Xie, Making Li-metal electrodes rechargeable by controlling the dendrite growth direction. *Nat. Energy* **2**, 17083 (2017).
- X. Wang, W. Zeng, L. Hong, W. Xu, H. Yang, F. Wang, H. Duan, M. Tang, H. Jiang, Stress-driven lithium dendrite growth mechanism and dendrite mitigation by electroplating on soft substrates. *Nat. Energy* **3**, 227–235 (2018).
- M. J. Zachman, Z. Tu, S. Choudhury, L. A. Archer, L. F. Kourkoutis, Cryo-STEM mapping of solid-liquid interfaces and dendrites in lithium-metal batteries. *Nature* **560**, 345–349 (2018).
- H. Wang, D. Lin, Y. Liu, Y. Li, Y. Cui, Ultrahigh-current density anodes with interconnected Li metal reservoir through overlithiation of mesoporous AlF₃ framework. *Sci. Adv.* **3**, e1701301 (2017).
- L. Fan, H. L. Zhuang, W. Zhang, Y. Fu, Z. Liao, Y. Lu, Stable lithium electrodeposition at ultra-high current densities enabled by 3D PMF/Li composite anode. *Adv. Energy Mater.* **8**, 1703360 (2018).
- S. Jin, Y. Jiang, H. Ji, Y. Yu, Advanced 3D current collectors for lithium-based batteries. *Adv. Mater.* **30**, 1802014 (2018).
- C. Zhang, S. Liu, G. Li, C. Zhang, X. Liu, J. Luo, Incorporating ionic paths into 3D conducting scaffolds for high volumetric and areal capacity, high rate lithium-metal anodes. *Adv. Mater.* **30**, 1801328 (2018).
- K. Liu, B. Kong, W. Liu, Y. Sun, M.-S. Song, J. Chen, Y. Liu, D. Lin, A. Pei, Y. Cui, Stretchable lithium metal anode with improved mechanical and electrochemical cycling stability. *Joule* **2**, 1857–1865 (2018).
- Y. An, H. Fei, G. Zeng, X. Xu, L. Ci, B. Xi, S. Xiong, J. Feng, Y. Qian, Vacuum distillation derived 3D porous current collector for stable lithium-metal batteries. *Nano Energy* **47**, 503–511 (2018).
- G. Li, Z. Liu, Q. Huang, Y. Gao, M. Regula, D. Wang, L.-Q. Chen, D. Wang, Stable metal battery anodes enabled by polyethylenimine sponge hosts by way of electrokinetic effects. *Nat. Energy* **3**, 1076–1083 (2018).
- D. Lin, J. Zhao, J. Sun, H. Yao, Y. Liu, K. Yan, Y. Cui, Three-dimensional stable lithium metal anode with nanoscale lithium islands embedded in ionically conductive solid matrix. *Proc. Natl. Acad. Sci. U.S.A.* **114**, 4613–4618 (2017).
- R. Zhang, X.-R. Chen, X. Chen, X.-B. Cheng, X. Q. Zhang, C. Yan, Q. Zhang, Lithiophilic sites in doped graphene guide uniform lithium nucleation for dendrite-free lithium metal anodes. *Angew. Chem. Int. Ed.* **56**, 7764–7768 (2017).
- H. Duan, J. Zhang, X. Chen, X.-D. Zhang, J.-Y. Li, L.-B. Huang, X. Zhang, J.-L. Shi, Y.-X. Yin, Q. Zhang, Y.-G. Guo, L. Jiang, L.-J. Wan, Uniform nucleation of lithium in 3D current collectors via bromide intermediates for stable cycling lithium metal batteries. *J. Am. Chem. Soc.* **140**, 18051–18057 (2018).
- X. Chen, X.-R. Chen, T.-Z. Hou, B.-Q. Li, X.-B. Cheng, R. Zhang, Q. Zhang, Lithiophilicity chemistry of heteroatom-doped carbon to guide uniform lithium nucleation in lithium metal anodes. *Sci. Adv.* **5**, eaau7728 (2019).
- F. Qiu, X. Li, H. Deng, D. Wang, X. Mu, P. He, H. Zhou, A concentrated ternary-salts electrolyte for high reversible Li metal battery with slight excess Li. *Adv. Energy Mater.* **9**, 1803372 (2018).
- X.-Q. Zhang, X.-B. Cheng, X. Chen, C. Yan, Q. Zhang, Fluoroethylene carbonate additives to render uniform Li deposits in lithium metal batteries. *Adv. Funct. Mater.* **27**, 1605989 (2017).
- H. Dai, K. Xi, X. Liu, C. Lai, S. Zhang, Cationic surfactant-based electrolyte additives for uniform lithium deposition via lithiophobic repulsion mechanisms. *J. Am. Chem. Soc.* **140**, 17515–17521 (2018).
- S. Komaba, T. Itabashi, M. Watanabe, H. Groult, N. Kumagai, Electrochemistry of graphite in Li and Na salt codissolving electrolyte for rechargeable batteries. *J. Electrochem. Soc.* **154**, A322–A330 (2007).
- W. Li, H. Yao, K. Yan, G. Zheng, Z. Liang, Y.-M. Chiang, Y. Cui, The synergetic effect of lithium polysulfide and lithium nitrate to prevent lithium dendrite growth. *Nat. Commun.* **6**, 7436 (2015).
- C. Yan, X.-B. Cheng, Y.-X. Yao, X. Shen, B.-Q. Li, W.-J. Li, R. Zhang, J.-Q. Huang, H. Li, Q. Zhang, An armored mixed conductor interphase on a dendrite-free lithium-metal anode. *Adv. Mater.* **30**, 1804461 (2018).
- W. Liu, D. Lin, A. Pei, Y. Cui, Stabilizing lithium metal anodes by uniform Li-ion flux distribution in nanochannel confinement. *J. Am. Chem. Soc.* **138**, 15443–15450 (2016).
- K. Yan, H.-W. Lee, T. Gao, G. Zheng, H. Yao, H. Wang, Z. Lu, Y. Zhou, Z. Liang, Z. Liu, S. Chu, Y. Cui, Ultrathin two-dimensional atomic crystals as stable interfacial layer for improvement of lithium metal anode. *Nano Lett.* **14**, 6016–6022 (2014).
- X.-B. Cheng, M.-Q. Zhao, C. Chen, A. Pentecost, K. Maleski, T. Mathis, X.-Q. Zhang, Q. Zhang, J. Jiang, Y. Gogotsi, Nanodiamonds suppress the growth of lithium dendrites. *Nat. Commun.* **8**, 336 (2017).
- D.-J. Yoo, S. Yang, Y. S. Yun, J. H. Choi, D. Yoo, K. J. Kim, J. W. Choi, Tuning the electron density of aromatic solvent for stable solid-electrolyte-interphase layer in carbonate-based lithium metal batteries. *Adv. Energy Mater.* **8**, 1802365 (2018).
- M. S. Kim, J.-H. Ryu, Deepika, Y. R. Lim, I. W. Nah, K.-R. Lee, L. A. Archer, W. I. Cho, Langmuir-Blodgett artificial solid-electrolyte interphases for practical lithium metal batteries. *Nat. Energy* **3**, 889–898 (2018).
- X. Han, Y. Gong, K. K. Fu, X. He, G. T. Hitz, J. Dai, A. Pearce, B. Liu, H. Wang, G. Rubloff, Y. Mo, V. Thangadurai, E. D. Wachsman, L. Hu, Negating interfacial impedance in garnet-based solid-state Li metal batteries. *Nat. Mater.* **16**, 572–579 (2017).
- Y. Liu, D. Lin, Y. Jin, K. Liu, X. Tao, Q. Zhang, X. Zhang, Y. Cui, Transforming from planar to three-dimensional lithium with flowable interphase for solid lithium metal batteries. *Sci. Adv.* **3**, eaao0713 (2017).
- J. Xie, J. Wang, H. R. Lee, K. Yan, Y. Li, F. Shi, W. Huang, A. Pei, G. Chen, R. Subbaraman, J. Christensen, Y. Cui, Engineering stable interfaces for three-dimensional lithium metal anodes. *Sci. Adv.* **4**, eaat5168 (2018).
- Q. Zhang, Y. Lu, L. Miao, Q. Zhao, K. Xia, J. Liang, S.-L. Chou, J. Chen, An alternative to lithium metal anodes: Non-dendritic and highly reversible sodium metal anodes for Li-Na hybrid batteries. *Angew. Chem. Int. Ed.* **57**, 14796–14800 (2018).
- K. Yan, Z. Lu, H.-W. Lee, F. Xiong, P.-C. Hsu, Y. Li, J. Zhao, S. Chu, Y. Cui, Selective deposition and stable encapsulation of lithium through heterogeneous seeded growth. *Nat. Energy* **1**, 16010 (2016).
- J. Zhao, L. Liao, F. Shi, T. Lei, G. Chen, A. Pei, J. Sun, K. Yan, G. Zhou, J. Xie, C. Liu, Y. Li, Z. Liang, Z. Bao, Y. Cui, Surface fluorination of reactive battery anode materials for enhanced stability. *J. Am. Chem. Soc.* **139**, 11550–11558 (2017).
- J. Xie, L. Liao, Y. Gong, Y. Li, F. Shi, A. Pei, J. Sun, R. Zhang, B. Kong, R. Subbaraman, J. Christensen, Y. Cui, Stitching h-BN by atomic layer deposition of LiF as a stable interphase for lithium metal anode. *Sci. Adv.* **3**, eaao3170 (2017).
- S. Komaba, N. Kumagai, Y. Kataoka, Influence of manganese(II), cobalt(II), and nickel(II) additives in electrolyte on performance of graphite anode for lithium-ion batteries. *Electrochim. Acta* **47**, 1229–1239 (2002).
- T. Ichitubo, S. Yagi, R. Nakamura, Y. Ichikawa, S. Okamoto, K. Sugimura, T. Kawaguchi, A. Kitada, M. Oishi, T. Doid, E. Matsuura, A new aspect of chevreol compounds as positive electrodes for magnesium batteries. *J. Mater. Chem. A* **2**, 14858–14866 (2014).
- Y. Cheng, H. J. Chang, H. Dong, D. Choi, V. L. Sprenkle, J. Liu, Y. Yao, G. Li, Rechargeable Mg-Li hybrid batteries: Status and challenges. *J. Mater. Res.* **31**, 3125–3141 (2016).
- Y. Li, W. Huang, Y. Li, A. Pei, D. T. Boyle, Y. Cui, Correlating structure and function of battery interphases at atomic resolution using cryoelectron microscopy. *Joule* **2**, 2167–2177 (2018).

46. Y. Liu, D. Lin, Y. Li, G. Chen, A. Pei, O. Nix, Y. Li, Y. Cui, Solubility-mediated sustained release enabling nitrate additive in carbonate electrolytes for stable lithium metal anode. *Nat. Commun.* **9**, 3656 (2018).
47. Y. Li, Y. Li, A. Pei, K. Yan, Y. Sun, C.-L. Wu, L.-M. Joubert, R. Chin, A. L. Koh, Y. Yu, J. Perrino, B. Butz, S. Chu, Y. Cui, Atomic structure of sensitive battery materials and interfaces revealed by cryo-electron microscopy. *Science* **358**, 506–510 (2017).
48. S. Liu, X. Xia, Y. Zhong, S. Deng, Z. Yao, L. Zhang, X.-B. Cheng, X. Wang, Q. Zhang, J. Tu, 3D TiC/C core/shell nanowire skeleton for dendrite-free and long-life lithium metal anode. *Adv. Energy Mater.* **8**, 1702322 (2018).
49. P. Albertus, S. Babinec, S. Litzelman, A. Newman, Status and challenges in enabling the lithium metal electrode for high-energy and low-cost rechargeable batteries. *Nat. Energy* **3**, 16–21 (2018).
50. L. Yu, S. Chen, H. Lee, L. Zhang, M. H. Engelhard, Q. Li, S. Jiao, J. Liu, W. Xu, J.-G. Zhang, A localized high-concentration electrolyte with optimized solvents and lithium difluoro(oxalate)borate additive for stable lithium metal batteries. *ACS Energy Lett.* **3**, 2059–2067 (2018).
51. P. Xue, S. Liu, X. Shi, C. Sun, C. Lai, Y. Zhou, D. Sui, Y. Chen, J. Liang, A hierarchical silver-nanowire-graphene host enabling ultrahigh rates and superior long-term cycling of lithium-metal composite anodes. *Adv. Mater.* **30**, 1804165 (2018).
52. S. Huang, W. Zhang, H. Ming, G. Cao, L.-Z. Fan, H. Zhang, Chemical energy release driven lithiophilic layer on 1 m² commercial brass mesh toward highly stable lithium metal batteries. *Nano Lett.* **19**, 1832–1837 (2019).
53. N. Li, W. Wei, K. Xie, J. Tan, L. Zhang, X. Luo, K. Yuan, Q. Song, H. Li, C. Shen, E. M. Ryan, L. Liu, B. Wei, Suppressing dendritic lithium formation using porous media in lithium metal-based batteries. *Nano Lett.* **18**, 2067–2073 (2018).
54. W. Zhang, H. L. Zhuang, L. Fan, L. Gao, Y. Lu, A “cation-anion regulation” synergistic anode host for dendrite-free lithium metal batteries. *Sci. Adv.* **4**, eaar4410 (2018).
55. P. Zhai, T. Wang, W. Yang, S. Cui, P. Zhang, A. Nie, Q. Zhang, Y. Gong, Uniform lithium deposition assisted by single-atom doping toward high-performance lithium metal anodes. *Adv. Energy Mater.* **9**, 1804019 (2019).
56. H. Qiu, T. Tang, M. Asif, X. Huang, Y. Hou, 3D porous Cu current collectors derived by hydrogen bubble dynamic template for enhanced Li metal anode performance. *Adv. Funct. Mater.* **29**, 1808468 (2019).
57. X.-B. Cheng, T.-Z. Hou, R. Zhang, H.-J. Peng, C.-Z. Zhao, J.-Q. Huang, Q. Zhang, Dendrite-free lithium deposition induced by uniformly distributed lithium ions for efficient lithium metal batteries. *Adv. Mater.* **28**, 2888–2895 (2016).

Acknowledgments

Funding: We acknowledge financial support by the National Natural Science Foundation of China (grant nos. 51722210, 51972285, U1802254, 51871201, and 51677170), and the Natural Science Foundation of Zhejiang Province (grant nos. LY16E070004 and LD18E020003). X.W.L. acknowledges the funding support from the National Research Foundation (NRF) of Singapore via the NRF Investigatorship (NRF-NRFI2016-04). **Author contributions:** H.Y., J.N., X.T., and X.W.L. conceived the idea and co-wrote the manuscript. H.Y. designed and performed the experiments and analyzed the data. H.T. and Z.J. assisted in TEM characterizations for materials. W.Z. and Y.L. contributed to interpreting the mechanism. All authors discussed the results and commented on the manuscript. **Competing interests:** The authors declare that they have no competing interests. **Data and materials availability:** All data needed to evaluate the conclusions in the paper are present in the paper and/or the Supplementary Materials. Additional data related to this paper may be requested from the authors.

Submitted 29 August 2019

Accepted 13 December 2019

Published 6 March 2020

10.1126/sciadv.aaz3112

Citation: H. Yuan, J. Nai, H. Tian, Z. Ju, W. Zhang, Y. Liu, X. Tao, X. W. Lou, An ultrastable lithium metal anode enabled by designed metal fluoride spansules. *Sci. Adv.* **6**, eaaz3112 (2020).